



NOVA

University of Newcastle Research Online

nova.newcastle.edu.au

Chen, Wei; Roberts, Alan; Katterfeld, Andre & Wheeler, Craig. "Modelling the stability of iron ore bulk cargoes during marine transport" Published in *Powder Technology*, Vol. 326, Issue February, p. 255-264, (2018).

Available from: <http://dx.doi.org/10.1016/j.powtec.2017.12.006>

© 2018. This manuscript version is made available under the CC-BY-NC-ND 4.0 license <http://creativecommons.org/licenses/by-nc-nd/4.0/>.

Accessed from: <http://hdl.handle.net/1959.13/1390093>

MODELLING THE STABILITY OF IRON ORE BULK CARGOES DURING MARINE TRANSPORTWei Chen^{1*}, Alan Roberts¹, Andre Katterfeld² and Craig Wheeler¹¹Centre for Bulk Solids and Particulate Technologies, The University of Newcastle, Callaghan, Australia 2308²Otto von Guericke University of Magdeburg, Magdeburg, Germany 39106

ABSTRACT: The safe maritime transport of bulk commodities, such as iron ore, by large bulk carriers is vitally dependent on the stability of the cargo. During transport there is a propensity that cargo shift may be triggered under the vessel's rolling motion. The study presented in this paper aims to model the critical stress conditions within iron ore bulk cargoes from a bulk solids flow perspective, from which the maximum roll angle of the vessel prior to cargo slip can be predicted. Comparison of the new theoretical approach to the classic slope stability model was conducted with similar results achieved. The influence of the failed material mass after the cargo slip event on the overall cargo stability is then examined using the discrete element method. The new theoretical and numerical approaches provide a means to predict the stability and evaluate the potential safety hazards during maritime transport of iron ore bulk cargoes.

KEYWORDS: Iron Ore; Cargo Stability; Cargo Slip; Bulk Solids; Discrete Element Modelling

1. INTRODUCTION

A subject of particular importance to the resources industry concerns the safe trans-oceanic transport of large tonnages of iron ore [1]. It is most important that the stability of the loaded bulk cargo be guaranteed under all dynamic conditions due to the rolling and pitching motion of the vessel induced by waves. Historically, many vessels transporting iron ore bulk cargoes have listed or capsized, with cargo shift being the suspected cause [2]–[6]. Therefore, safety precautions are urgently required during shipping the iron ore bulk materials. As shown in Figure 1, there are two main failure modes that result in cargo shift, namely, liquefaction and cargo slip [7], [8].

Figure 1. Two different modes of cargo shift during iron ore maritime transport.

Liquefaction occurs due to the cyclic motion of the ship and may lead to the loss of shear strength, and subsequent cargo shift [4], [9]. Liquefaction of an iron ore bulk cargo is a process where the bulk material flows in a manner resembling a liquid under the monotonic or cyclic ship motion. Under the regulation of the International Maritime Solid Bulk Cargo Code (IMSBC Code) [10], a Transportable Moisture Limit (TML) test shall be conducted on all eligible iron ore fines commodities to determine the upper moisture threshold for safe maritime transport. If an iron ore cargo is eligible for a TML, the gross water content of the material on board the vessel must not exceed the TML value to eliminate the risk of liquefaction.

In comparison, cargo slip involves a portion of the surcharge zone within the stockpile, and it is often argued that it poses less danger to the stability of the vessel [11]. The failure mechanism is predominantly related to the material's stress state under dynamic ship motion [12]. The cargo slip phenomenon alters the vessel's metacentre leading to instability of the bulk carrier. Kirby [13] suggests a circular shear failure surface for cohesive iron ore fines on the basis of the classic slope stability theory in soil mechanics. Recent studies [14] have investigated the motion experienced by various vessel classes, which provides further details to better predict and assess the cargo stability.

Based on the forgoing comments, the study presented in this paper aims to address the cargo slip phenomenon during maritime transport of iron ore using analytical and numerical methods to predict cargo slip and assess post-failure stability.

2. CARGO SLIP MODELLING – BULK SOLIDS FLOW THEORY

Generally, an iron ore bulk cargo is constrained on five boundaries with only the top surface free. The load profile is dependent on the shape of the hold, the hatch arrangement and the degree of fill, while the surface of the bulk material is often rilled to form a surcharge angle (θ_s). It is assumed that the moisture content of the bulk material is below saturation level and, therefore, the bulk solid can be described as a Coulomb friction, cohesive material [15]. Figure 2 shows typical material properties of an iron ore product, including particle density, bulk density and particle size distribution.

Figure 2. Particle density, bulk density and particle size distribution of a 7.9% moisture content iron ore sample.

The stress condition exhibited by bulk solids can be analysed using a Hvorslev-Roscoe yield surface [16], [17], as shown in Figure 3. When a sample is consolidated to the critical state under a nominated major consolidation stress σ_1 , the material exhibits unconfined yield stress σ_c and cohesion stress τ_c , along with a static internal frictional angle ϕ_t and an effective frictional angle δ . These stress state parameters are often obtained through a Jenike direct shear test [18], [19]. Figure 4 shows the flow property results for the iron ore discussed above.

Figure 3. Stress conditions at critical state within the bulk solids.

Figure 4. Flow properties of an iron ore sample with 7.9% moisture content; (a) Unconfined yield strength and cohesion stress; (b) Static and effective internal friction angles.

Based on the flow properties of the iron ore material, modelling of the cargo slip within a bulk cargo is performed as follows. As shown in Figure 5, for an infinitesimal element located on the potential

shear plane within a cargo hold exhibiting a roll angle of θ_R , σ_1 and σ_2 are the major and minor principal stresses applied to the element. It is assumed that an active stress state exists, and σ_1 acts vertically and is equal to the hydrostatic pressure:

$$(1) \quad \sigma_1 = \rho_B g y$$

Where ρ_B is the bulk density, g is acceleration due to gravity and y is the depth below the load profile surface.

In the Mohr diagram of Figure 5 (b), the point of intersection (Point A) of the yield locus with the Mohr semi-circle through σ_1 and σ_2 defines the stress condition at failure with σ_β being the normal stress and τ_β being the shear stress acting on the plane of failure which is inclined at an angle β to the plane of the major principal stress.

Figure 5. Cargo slip modelling within the cargo hull; (a) stress conditions on the possible plane of failure; (b) stress state of the material in Mohr circle diagram.

Based on the diagram in Figure 5 (a), the following relationships can be derived:

$$(2) \quad \sigma_\beta = \frac{\sigma_1}{1+\sin\delta} [1 - \sin\phi_{ti}\sin\delta]$$

$$(3) \quad \tau_\beta = \frac{\sigma_1}{1+\sin\delta} [\cos\phi_{ti}\sin\delta]$$

Where δ is the effective angle of internal friction and ϕ_{ti} is the initial static angle of internal friction. Given the normal stress σ_β and the shear stress τ_β , the following correlation is established,

$$(4) \quad \phi_f = \arctan \frac{\tau_\beta}{\sigma_\beta}$$

Substituting Eq. (2) and Eq. (3) into Eq. (4), the following equivalent frictional angle is obtained,

$$(5) \quad \phi_f = \arctan \left[\frac{\cos\phi_{ti}\sin\delta}{1-\sin\phi_{ti}\sin\delta} \right]$$

The equivalent friction angle establishes the criterion when the free flowing behaviour of the material occurs. Therefore, cargo slip is predicted when the yield plane exceeds an angle of:

$$(6) \quad \phi_f = \theta_R + \theta_a + \theta_s$$

Where θ_R is the roll angle of the vessel, and θ_a is an additional angle due to the rolling acceleration. A value of $\theta_a = 5^\circ$ is often selected [13], [20]. The combination of θ_R and θ_a may be considered as the effective roll angle of the vessel at which the cargo is likely to slip. The yield plane angle ϕ_f is dependent on the material's flow properties. Figure 6 shows the critical roll angle as a function of the major consolidation stress using the flow property results of the typical iron ore fines material shown in Figure 2 and Figure 4. The reduction of the maximum roll angle is directly related to the effective and static friction angles as indicated by Eq. (5) and Eq. (6).

Figure 6. Maximum roll angles and failure depth below load surface for cargo slip as a function of major consolidation stress for an iron ore stockpile with a surcharge angle of 30°.

3. CARGO SLIP MODEL – THE SLOPE STABILITY THEORY

Kirby [13] utilised the classical theory for slope stability in soil mechanics to model the cargo slip phenomenon. Considering a cohesive iron ore cargo shown in Figure 7 (a), modelling was performed by considering the effect of gravity to shift the cargo when it is at a rolling level. The material burden is deemed to fail along a circular surface when the gravitational force due to rolling exceeds the resistant shear force. Despite that this method and the flow property theory were both developed based on the stress state of the cargo, the slope stability theory assumes a fixed arrangement of the cargo load profile.

Kirby [13] derived a cargo slip model based on the effective roll angle of the vessel ($\theta_r + \theta_a$), the static frictional angle (φ_t) of the bulk material and a non-dimensional parameter N to determine the maximum slope angle of a cargo. The non-dimensional parameter N is defined as:

$$(7) \quad N = \frac{\tau_c}{\rho_B g L}$$

Where

- τ_c is the cohesion stress exhibited by the bulk solids
- ρ_B is the bulk density
- g is the gravitational acceleration
- L is the slope length

The model above leads to a suite of cargo safety design charts. The design charts were derived for bulk solids with a wide range of friction angles under a specific effective rolling angle (static rolling angle plus 5° rolling acceleration effect). The design chart for an effective roll angle of 20° is shown in Figure 7 (b). The modelling procedure commences with a nominated effective roll angle for a vessel. Providing the stockpile within the cargo hold is loaded with a similar surcharge arrangement as per Figure 7 (a), the non-dimensional factor N for a bulk material with a known cohesion stress (τ_c) and bulk density (ρ_B) is obtained. With the resulting non-dimensional factor N and the static friction angle (φ_t), the maximum safe surcharge angle θ_s is obtained.

Figure 7. Cargo slip modelling based on the slope stability theory [13].

The two forgoing modelling methods are able to predict the critical roll angle at which the cargo slip is likely to slip, with each model potentially leading to a different amount of material movement. The

actual influence on the overall cargo stability (centre of gravity shift) after cargo slip is not considered. The re-distribution of the failed material mass may significantly alter the centre of gravity of the vessel, causing stability issues. This study aims to assess the stability of the vessel post cargo slip using discrete element modelling.

4. DEM MODELLING OF THE CARGO STABILITY

Discrete element modelling (DEM) is an ideal tool to study cargo stability post slip by analysing the post failure material redistribution. The DEM code used in this study was LIGGGHTS [21]. The Hertz-Mindlin model (Cundall & Strack, 1979) was used to compute the particle-particle and particle-wall contacts. The contact force between two particles includes a normal force (F_n) component and a tangential force (F_t) component,

$$(8) \quad \mathbf{F} = \mathbf{F}_n + \mathbf{F}_t$$

$$\mathbf{F} = (k_n \delta \mathbf{n}_{ij} - \gamma_n \mathbf{v} \mathbf{n}_{ij}) + (k_t \delta \mathbf{t}_{ij} - \gamma_t \mathbf{v} \mathbf{t}_{ij})$$

Where

- F_n is the normal contact force,
- F_t is the tangential contact force,
- k_n is the elastic constant for normal contact,
- $\delta \mathbf{n}_{ij}$ is the normal overlap,
- γ_n is the viscoelastic damping constant for normal contact,
- $\mathbf{v} \mathbf{n}_{ij}$ is the normal relative velocity (normal component of the relative velocity of the two particles),
- k_t is the elastic constant for tangential contact,
- $\delta \mathbf{t}_{ij}$ is the tangential overlap,
- γ_t is the viscoelastic damping constant for tangential contact,
- $\mathbf{v} \mathbf{t}_{ij}$ is the tangential relative velocity (tangential component of the relative velocity of the two particles).

Static friction is obtained by tracking the elastic shear displacement throughout the period of the contact. The tangential overlap $\delta \mathbf{t}_{ij}$ is truncated when necessary to fulfil a local Coulomb yield criterion: $F_t \leq \mu F_n$, where μ is the particle-particle friction coefficient. Therefore, there is assumed to be no relative movements between contact surfaces when $F_t > \mu F_n$, and when the Coulomb yield criterion is satisfied the contact surfaces slip relatively to each other.

The normal force has two terms, a spring force and a damping force. The tangential force also has two terms: a shear force and a damping force. The shear force is a “history” effect that accounts for the tangential displacement (tangential overlap) between the particles for the duration of the time they are in contact.

Considering that the shear modulus (G) can be calculated from Young's modulus and Poisson's ratio, the Hertz-Mindlin contact model depends on the following material parameters:

- Coefficient of restitution, e
- Young's modulus, Y
- Poisson ratio, ν
- Coefficient of static friction, μ_s
- Coefficient of rolling friction, μ_r

The contact model coefficients in Eq. (8) were calculated as follows,

$$(9) \quad k_n = \frac{4}{3} Y^* \sqrt{R^* \delta_n}$$

$$(10) \quad \gamma_n = -2 \sqrt{\frac{5}{6}} \beta \sqrt{S_n m^*} \geq 0$$

$$(11) \quad k_t = 8G^* \sqrt{R^* \delta_n}$$

$$(12) \quad \gamma_t = -2 \sqrt{\frac{5}{6}} \beta \sqrt{S_t m^*} \geq 0$$

where

$$(13) \quad S_n = 2Y^* \sqrt{R^* \delta_n}$$

$$(14) \quad S_t = 8G^* \sqrt{R^* \delta_n}$$

$$(15) \quad \beta = \frac{\ln(e)}{\sqrt{\ln^2(e) + \pi^2}}$$

$$(16) \quad \frac{1}{Y^*} = \frac{(1-\nu_1^2)}{Y_1} + \frac{(1-\nu_2^2)}{Y_2}$$

$$(17) \quad \frac{1}{G^*} = \frac{2(2+\nu_1)(1-\nu_1)}{Y_1} + \frac{2(2+\nu_2)(1-\nu_2)}{Y_2}$$

$$(18) \quad \frac{1}{R^*} = \frac{1}{R_1} + \frac{1}{R_2}$$

$$(19) \quad \frac{1}{m^*} = \frac{1}{m_1} + \frac{1}{m_2}$$

where e is the coefficient of restitution, m is the mass and R is the radius of a particle. The subscripts 1 and 2 denote to the two particles in contact.

Additionally, when the rolling resistance is selected for the contacts, the elastic-plastic spring-dashpot (EPSD) model [23] is utilised. This model adds an additional torque contribution in an incremental way by the following;

$$(20) \quad M_{r,t+\Delta t}^k = \begin{cases} M_{r,t}^k - k_r \omega_r \Delta t; & \text{if } |M_{r,t}^k - k_r \omega_r \Delta t| < \mu_r R^* |F_n| \\ \mu_r R^* |F_n| \frac{M_{r,t}^k - k_r \omega_r \Delta t}{|M_{r,t}^k - k_r \omega_r \Delta t|}; & \text{otherwise} \end{cases}$$

where

- $k_r = k_t R^{*2}$ is the rolling stiffness [24],

- ω_r is the relative angular velocity of the two particles in contact.

The EPSD rolling friction model also has a viscous damping component [23]. However, it is neglected in this study since the rolling stiffness model selected above can already provide the ideal case of a well behaved and well damped rolling resistance without the introduction of another hard-to-define parameter (viscous component) that may have an impact on the behaviour. [25].

4.1 DEM Calibration

Prior to conducting the full size cargo stability modelling, it is critical to ensure the modelling parameters can represent the physical behaviours of the actual material, therefore a DEM calibration process is essential [26], [27]. DEM calibration is designed to validate a set of nominated material parameters which manifests similar flow properties in the numerical environment compared to experiments.

In this study, a DEM calibration system shown in Figure 8 (a) is developed. The experimental process is shown below:

- The material sample is continuously poured into the top hopper and flows down into the middle chamber. The middle chamber has a dimension of 500mm by 500mm and a front-back spacing of 100mm.
- When a stockpile is steadily formed in the mid chamber, a discharge gate with an opening of 200mm is opened to allow material to flow into the bottom chamber. At the end of the discharge, two shear angles (α_1 and α_2) are formed in the middle chamber.
- Two angles of repose (β_1 and β_2) will also form within the bottom chamber.

Figure 8. Discrete element modelling (DEM) calibration and optimal selection of the modelling parameters.

Considering the iron ore sample with material properties shown in Figure 2, the d_{50} of the sample is approximately 2.8mm. To perform the DEM modelling of the calibration test, a proper selection of the particle size is critical to ensure both correct material behaviours and realistic computational time in the full scale cargo modelling. Scale-up of both the particle size and calibration system are required to achieve a realistic computational turnaround time, as well as to ensure that the minimal geometry of the calibration system to be at least 5 times of the largest particle size to eliminate the wall effect. The scaled-up particle size and calibration system geometry selected in this study are shown in Table 1.

Table 1. Up-scaling of the discrete element modelling parameters.

An identical process is replicated in the DEM modelling, and the resulting shear angles and angles of repose are compared to the experimental results. The search for the DEM material parameters set is an optimisation process as shown in Figure 8 (b). By iterating the combination of various particle frictions (μ_s), and rolling frictions (μ_r), a comprehensive database of material behaviours is obtained. No cohesive contact is considered in the DEM calibration. This is due to the small cohesion stress exhibited by the material under low consolidation stress as shown in Figure 4. In addition, it is important to note that the current development of the discrete element modelling involves some degrees of idealisation, such as using coarse particles and limited size distribution. This leads to that realistic behaviours may be obtained in DEM calibration by increasing the frictional factors and not adding cohesion/adhesion [26], [28]–[30]. By this means, calibration of the cohesion parameter in DEM is eliminated. Obviously, if no realistic behaviour can be achieved by only tuning frictional parameters, cohesion may be added into the DEM calibration matrix.

The optimal parameter set is selected by closely matching the shear angles and angles of repose achieved in calibration tests. Apart from the forgoing parameters used in the optimisation study, all simulation parameters are maintained at values as shown in Table 2. Among these parameters, Poisson's ratio was determined by the particle's shear stiffness and normal stiffness [31]–[33]. The wall friction was selected as 0.3 [34] as the predominant of the contacts in the modelling is particle-to-particle. Regarding the coefficient of restitution, previous studies have suggested that coefficient of restitution has limited influence on the flow behaviour of bulk solids and a relatively low coefficient of restitution may be used for such bulk materials [35]. In addition, keeping the coefficient of restitution at a fixed value will eliminate one more parameter for DEM calibration.

Table 2. Parameters used for all discrete element modelling calibration simulation.

4.2 DEM Modelling of a Handy Size Vessel

When the optimum DEM parameters are obtained through calibration, the full size cargo stability modelling is performed. As outlined by the Iron Ore Technical Working Group [14], the Handy size vessel is likely to exhibit the greatest risk of cargo slip during transport, and therefore, is selected as the modelling case in this study. As shown in Figure 9, for a typical Handy size cargo hold, the nominal load limit for the cargo is 1,000 tonnes. Considering the typical iron ore material presented in Section 2 with a particle density of 4,800 kg/m³, this yields a total number of 3,183,099 mono-sized spheres 50mm in diameter. The actual modelling process follows the steps below:

- The cargo hold is centrally loaded with a mass flow rate of 16,000 t/hr, which takes 225 seconds simulation time
- Wait for 5 seconds until the stockpile is stabilised
- Rotate cargo 20° anti-clockwise in 5 seconds
- Rotate cargo 20° clockwise in 5 seconds and revert back to the original position

The rotational speed is adopted from the study conducted by the Iron Ore Technical Working Group, which argued that the rolling period of a vessel is 10 seconds. The calibrated material parameters together with the parameters in Table 2 were used for this modelling. During rolling, the movements of the particles are monitored to examine the maximum roll angle which triggers the cargo slip. The resulting centre of gravity shift is also evaluated with results discussed below.

Figure 9. Discrete element modelling (DEM) of a Handy size cargo hold. (a) cargo hold geometry; (b) rolling motion applied to the cargo hold after loaded.

5. RESULTS AND DISCUSSION

5.1 Cargo Slip Modelling Comparison

The cargo slip model using the bulk solids flow property theory and the slope stability theory (Kirby [13]) is compared based on the Handy size cargo geometry in the forgoing discussion. The iron ore sample with material properties shown in Figure 2 and Figure 4 are also utilised. For Kirby's model, the cargo geometry yields a slope length of 6m for a nominal stockpile surcharge angle of 30°. Following the assumption that the maximum roll angle is 20°, comprising of 15° static roll angle and 5° acceleration effect, the stockpile stress properties at the failure plane are calculated as:

- Failure plane depth $y = 3.46$ m
- Major consolidation stress $\sigma_1 = 89$ kPa
- Bulk Density $\rho_B = 2623$ kg/m³
- Static internal frictional angle $\varphi_t = 50^\circ$
- Unconfined yield strength $\sigma_c = 21.7$ kPa
- Cohesion stress $\tau_c = 4.1$ kPa

The conditions above yield a Kirby non-dimensional parameter N of 0.048, which corresponds to a maximum surcharge angle of 43.6°.

For comparison purposes, applying the bulk solids flow property theory, for the following stockpile parameters:

- An identical surcharge angle of 30°
- Major consolidation stress $\sigma_1 = 89$ kPa
- Bulk Density $\rho_B = 2623$ kg/m³
- Static internal frictional angle $\varphi_t = 50^\circ$
- Effective internal frictional angle $\delta = 53^\circ$
- Acceleration effect to rolling $\theta_a = 5^\circ$

This condition yields a maximum roll angle of 22.9°, with 17.9° static roll angle, being close to 15° as predicted by Kirby. Based on this comparison, the angle for initiating cargo slip are similar for both models.

5.2 DEM Calibration Results

The influence of the failed material mass on the stability of the vessel will now be assessed using DEM. The DEM calibration proposed in the forgoing discussion led to a total of 81 simulations. From this comprehensive shear angle and angle of repose database, the influence of the particle friction and the rolling friction on the material flow behaviours can be examined. As shown in Figure 10, it is evident that higher shear angles and larger angles of repose are obtained when increasing the particle friction and rolling friction. This indicates greater material strength is simulated when increasing these parameters.

Figure 10. Influence of the particle friction parameters on the material behaviour in the discrete element model; (a) shear angle results; (b) angle of repose results.

The shear angle and the angle of repose in each modelling case were measured and then compared with the experimental results. Out of the 81 modelling cases, the following parameters were found to closely match the experimental observations:

- Particle friction (μ_s): 0.7
- Rolling friction (μ_r): 0.6

A comparison between the experimental test and the DEM results is shown in Figure 11. It is evident that the selected parameters resulted in close correlation to the experiment. This parameter set was utilised for the full scale cargo modelling below.

Figure 11. Comparison between the experimental (left) shear angle and the angle of repose and the discrete element modelling results (right) using the optimised parameter set.

5.3 Stability for a Handy Size Cargo

The DEM modelling results of the full scale Handy size cargo are discussed below, for the rolling phase and the post cargo slip phase. As shown in Figure 12 (a), on completion of the loading sequence, the material formed a stockpile with an angle of repose around 33 to 35°. Once the rolling motion was initiated, the movement of the material within the stockpile was continuously monitored, and the cargo slip was observed to be initiated at a rolling angle of 16.0° as shown in Figure 12 (b). The side view of the cargo slip event is shown in Figure 12 (c). This angle lies between the value predicted

using the Kirby model and the bulk solids flow property theory as shown in **Table 3**. The shape of the predicted failure plane appears to be closer to that assumed by the bulk solids flow property theory.

Table 3. Static roll angles modelling results using the flow property theory, the slope stability theory and DEM.

The stockpile within the cargo after cargo slip is shown in Figure 12 (d). With the new positions of all particles, the centre of gravity post cargo slip is estimated to be 1.3m from the original stockpile centre of gravity. While the change in the centre of gravity may not result in significant cargo instability, and may be corrected by adjusting the vessel's ballast tank or additional cargo slips on the opposite side of the stockpile, it is paramount for the crew to understand the potential risk when transporting such bulk solids.

Figure 12. Discrete element modelling of the full size Handy size cargo; (a) stockpile formed after loading; (b) initiation of cargo slip – front view; (c) initiation of cargo slip – side view; (d) stockpile profile after cargo slip and new centre of gravity.

6. Conclusion

The study presented in this paper investigated the load stability of iron ore cargoes during maritime transport. Two analytical approaches and a numerical method were compared with the results yielding the following major conclusions:

- The bulk solids flow property theory can be utilised to model cargo slip during maritime transport of iron ore.
- The cargo slip predicted using the classic slope stability theory and bulk solids flow property theory provide similar results.
- The cargo slip predicted using the discrete element method showed similar results compared to the theoretical models
- The influence of the cargo slip on the centre of gravity can be assessed, with precaution and correction measures put in place to reduce vessel instability, such as ballast tank adjustment.

The results of this study have enhanced the understanding of a cargo slip event through modelling and have consequently provided a means to predict and assess potential safety hazards related to the maritime transport of iron ore.

Reference

- [1] AMIRA International, "P1097 - Systematic Evaluation of Transportable Moisture Limit Measurement Methods for Iron Ore Fines Bulk Cargoes - Public Final Report," 2014.

- [2] Australian Transport Safety Bureau, "Marine Safety Investigation Report 34: Loss of Bulk Carrier Melete," 1991.
- [3] Bulk Carrier Guide, "Causes of Iron Ore Liquefaction During Sea Passage & Countermeasures," 2010. [Online]. Available: <http://www.bulkcarrierguide.com/iron-ore-liquefaction-cases.html>.
- [4] C. Andrei and R. H. Pazara, "The impact of bulk cargoes liquefaction on ship's intact stability," *UPB Sci. Bull.*, vol. 75, no. 4, pp. 47–58, 2013.
- [5] B. Gallagher, S. Stogsdill, and R. W. Stephenson, "Influence of ore physical properties on the transportable moisture limit for barged materials," 2005.
- [6] L. A. van Paassen, P. J. Vardon, A. Mulder, G. van de Weg, and P. Jeffrey, "Investigating the susceptibility of iron ore to liquefaction," in *Poromechanics V: Proceedings of the Fifth Biot Conference on Poromechanics*, 2013, pp. 1478–1487.
- [7] K. L. Sandvik and A. Rein, "Safe transport at sea of bulk mineral cargoes," *Bulk Solids Handl.*, vol. 12, p. 79, 1992.
- [8] A. W. Roberts and O. J. Scott, "A Commentary on the Application of Bulk Solids Strength and Flow Properties to the Evaluation of the Conditions for the Safe Transport of Bulk Coal by Ship," ACARP Report R5-85-4138, 1985.
- [9] B. Seed and K. L. Lee, "Liquefaction of saturated sands during cyclic loading," *J. Soil Mech. Found. Div.*, vol. 92, no. ASCE# 4972 Proceeding, 1966.
- [10] International Maritime Organization, "International maritime solid bulk cargoes code," 2013.
- [11] N. Roberts, "Liquefaction and Bulk Carrier Total Losses: Key Issues," Joint Hull Committee, London, 2012.
- [12] H. Wang, J. Koseki, T. Sato, G. Chiaro, and J. T. Tian, "Effect of saturation on liquefaction resistance of iron ore fines and two sandy soils," *Soils Found.*, vol. 56, no. 4, pp. 732–744, 2016.
- [13] J. Kirby, "Shifts in Granular Bulk Mineral Cargoes: Why They Occur and How to Avoid Them," 1983.
- [14] Iron Ore Technical Working Group, "Marine Report," 2013.
- [15] B. Paul, *A modification of the Coulomb-Mohr theory of fracture*. Division of Engineering, Brown University, 1960.
- [16] M. J. Hvorslev, "Physical components of the shear strength of saturated clays.," DTIC Document, 1961.
- [17] K. H. Roscoe, An. Schofield, and C. P. Wroth, "On the yielding of soils," *Geotechnique*, vol. 8, no. 1, pp. 22–53, 1958.
- [18] W. Chen, A. Roberts, K. Williams, J. Miller, and J. Plinke, "On uniaxial compression and Jenike direct shear testings of cohesive iron ore materials," *Powder Technol.*, vol. 312, pp. 184–193, 2017.
- [19] ASTM International, "ASTM D6128, Standard test method for shear testing of bulk solids using the Jenike shear cell. ASTM International." West Conshohocken, PA, 2015.
- [20] P. V Green and T. H. Hughes, "Stability of bulk mineral cargoes," *Inst. Min. Metall. Sect A*, vol. 86, 1977.
- [21] C. Kloss and C. Goniva, "Liggghts—a new open source discrete Element simulation software," in *Proc. of The 5th International Conference on Discrete Element Methods*, 2010, pp. 25–26.
- [22] P. A. Cundall and O. D. L. Strack, "A discrete numerical model for granular assemblies," *Geotechnique*, vol. 29, no. 1, pp. 47–65, 1979.

- [23] J. Ai, J.-F. Chen, J. M. Rotter, and J. Y. Ooi, "Assessment of rolling resistance models in discrete element simulations," *Powder Technol.*, vol. 206, no. 3, pp. 269–282, 2011.
- [24] K. Iwashita and M. Oda, "Rolling resistance at contacts in simulation of shear band development by DEM," *J. Eng. Mech.*, vol. 124, no. 3, pp. 285–292, 1998.
- [25] C. M. Wensrich and A. Katterfeld, "Rolling friction as a technique for modelling particle shape in DEM," *Powder Technol.*, vol. 217, pp. 409–417, 2012.
- [26] A. Katterfeld, T. Donohue, and W. Chen, "On the Calibration of Material Properties for Discrete Element Modelling," in *ICBMH 2013 - 11th International Conference on Bulk Materials Storage, Handling and Transportation*, 2013.
- [27] T. Gröger and A. Katterfeld, "On the numerical calibration of discrete element models for the simulation of bulk solids," *Comput. Aided Chem. Eng.*, vol. 21, pp. 533–538, 2006.
- [28] M. Rahman, D. L. Schott, A. Katterfeld, and C. M. Wensrich, "Influence of the software on the calibration parameters for DEM simulations," *Bulk Solids Handl.*, vol. 31, no. 7–8, pp. 396–400, 2011.
- [29] A. P. Grima and P. W. Wypych, "Investigation into calibration of discrete element model parameters for scale-up and validation of particle–structure interactions under impact conditions," *Powder Technol.*, vol. 212, no. 1, pp. 198–209, 2011.
- [30] T. Roessler and A. Katterfeld, "Scalability of angle of repose tests for the calibration of DEM parameters," in *12th International Conference on Bulk Materials Storage, Handling and Transportation (ICBMH 2016), The*, 2016, p. 201.
- [31] A. C. Collop, G. R. McDowell, and Y. W. Lee, "Modelling dilation in an idealised asphalt mixture using discrete element modelling," *Granul. Matter*, vol. 8, no. 3, pp. 175–184, 2006.
- [32] M. Rackl, C. D. Görnig, K. J. Hanley, and W. A. Günthner, "Efficient calibration of discrete element material model parameters using latin hypercube sampling and kriging," in *Proceedings of ECCOMAS*, 2016.
- [33] M. Rackl and K. J. Hanley, "A methodical calibration procedure for discrete element models," *Powder Technol.*, vol. 307, pp. 73–83, 2017.
- [34] C. J. Coetzee and D. N. J. Els, "Calibration of discrete element parameters and the modelling of silo discharge and bucket filling," *Comput. Electron. Agric.*, vol. 65, no. 2, pp. 198–212, 2009.
- [35] C. M. Wensrich and A. Katterfeld, "Rolling friction as a technique for modelling particle shape in DEM," *Powder Technol.*, vol. 217, pp. 409–417, Feb. 2012.

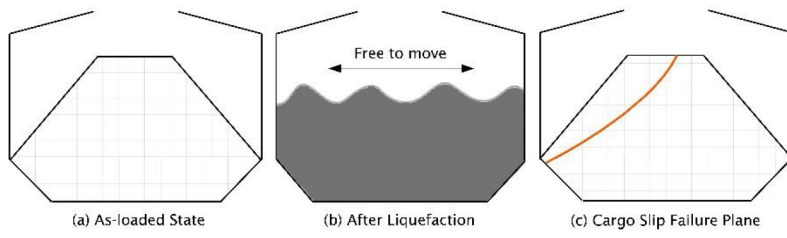


Figure 1

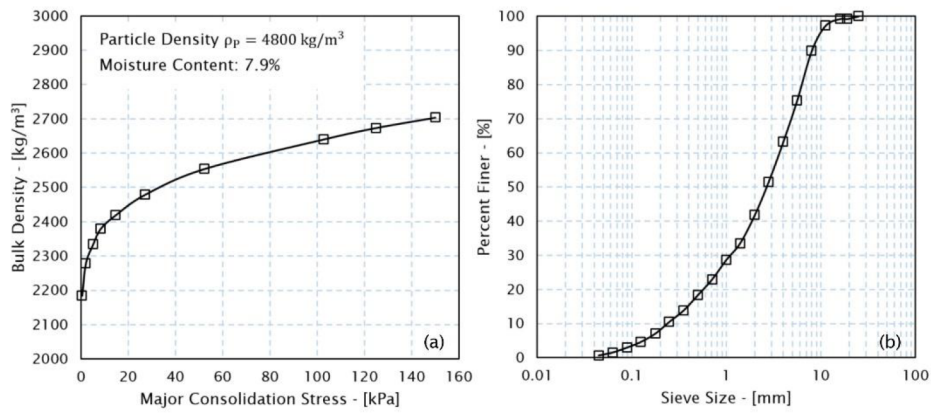


Figure 2

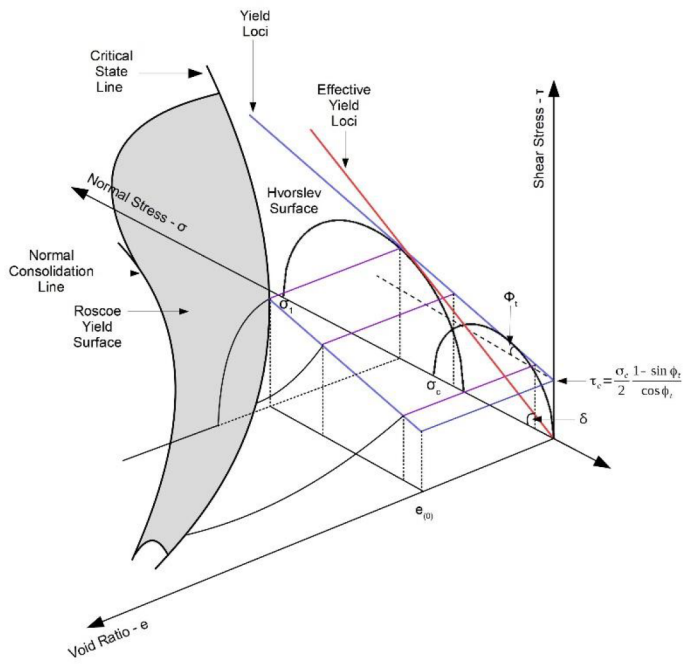


Figure 3

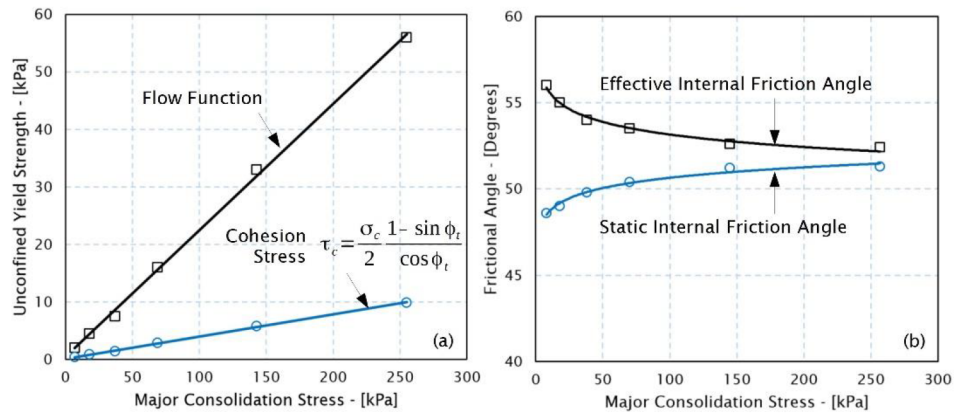


Figure 4

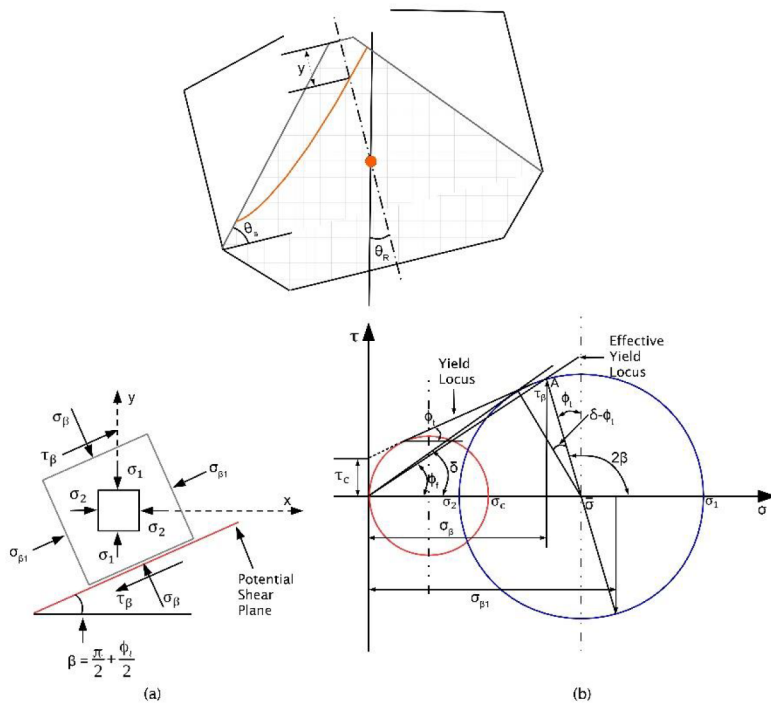


Figure 5

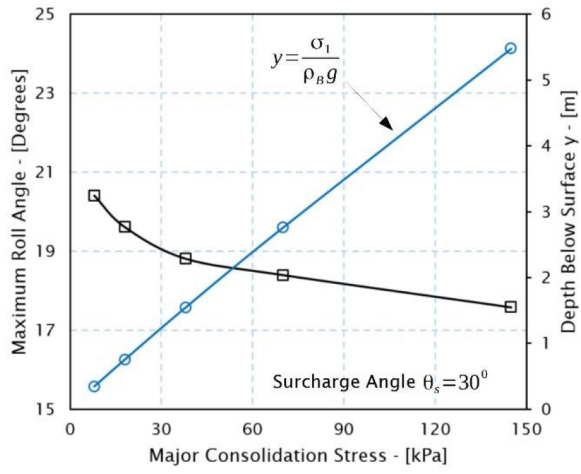


Figure 6

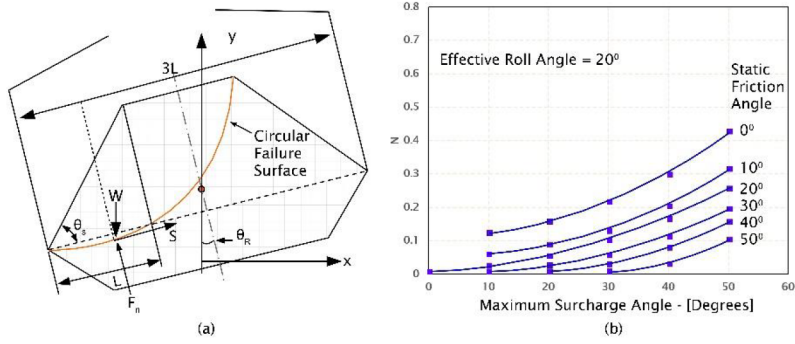


Figure 7

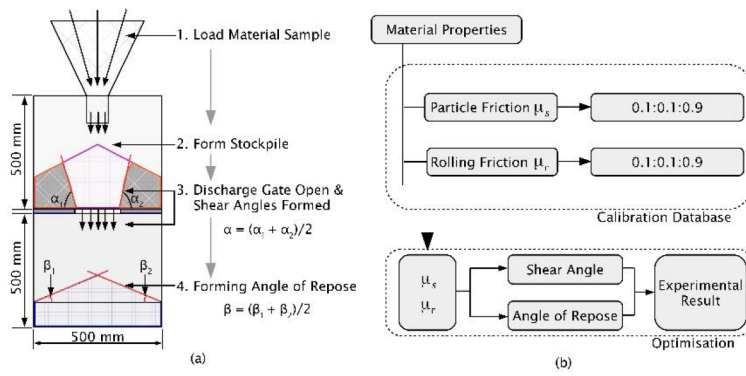


Figure 8

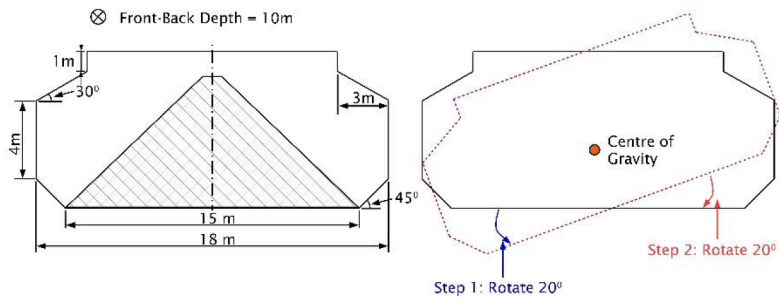


Figure 9

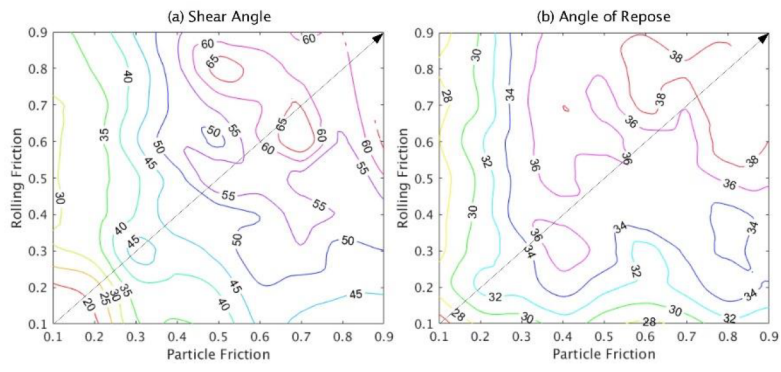


Figure 10

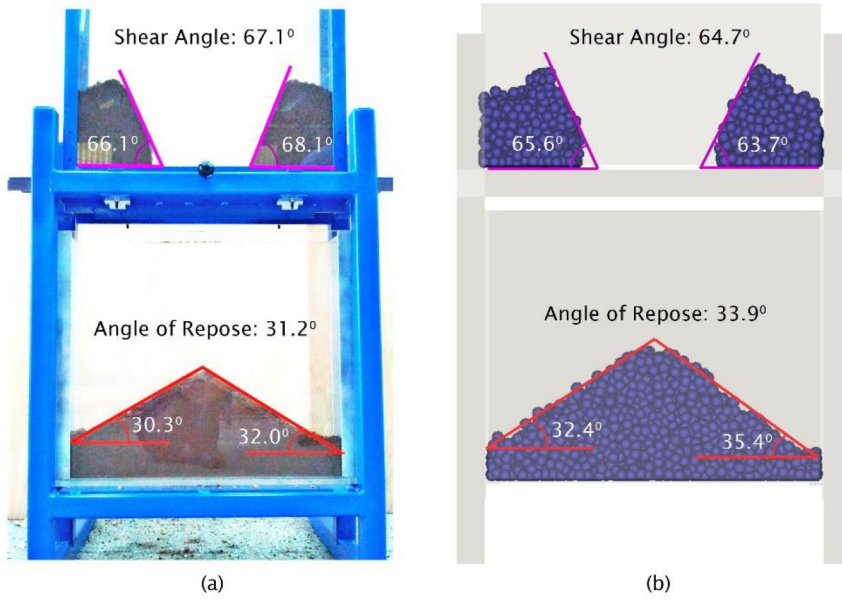


Figure 11

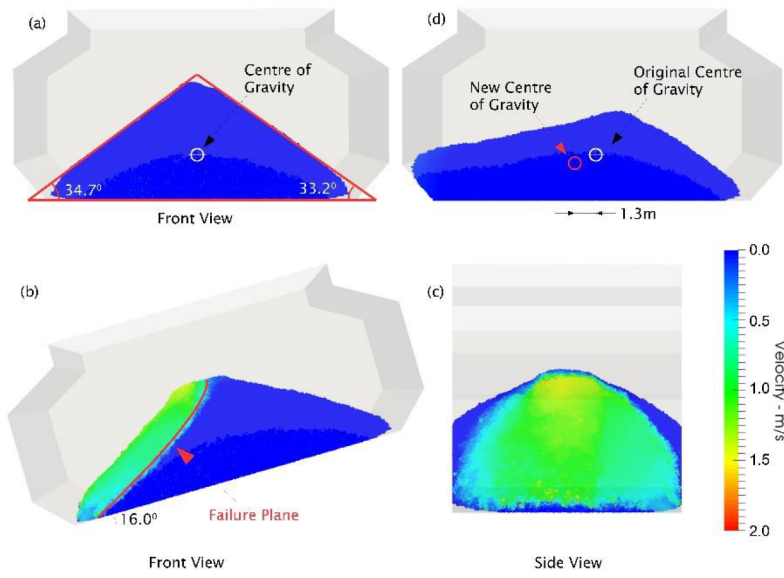


Figure 12

Table 1. Up-scaling of the discrete element modelling parameters.

	Experiment	Scaled
Particle Size - mm	2.8	50 (Mono-sized Sphere)
Total Mass - kg	50	1,000
Mid Chamber Dimension - mm	500 (Width) 500 (Height) 100 (Front-Back)	2500 (Width) 2500 (Height) 500 (Front-Back)
Discharge Gate	200	1000
Bottom Chamber Dimension - mm	500 (Width) 500 (Height) 100 (Front-Back)	2500 (Width) 2500 (Height) 500 (Front-Back)

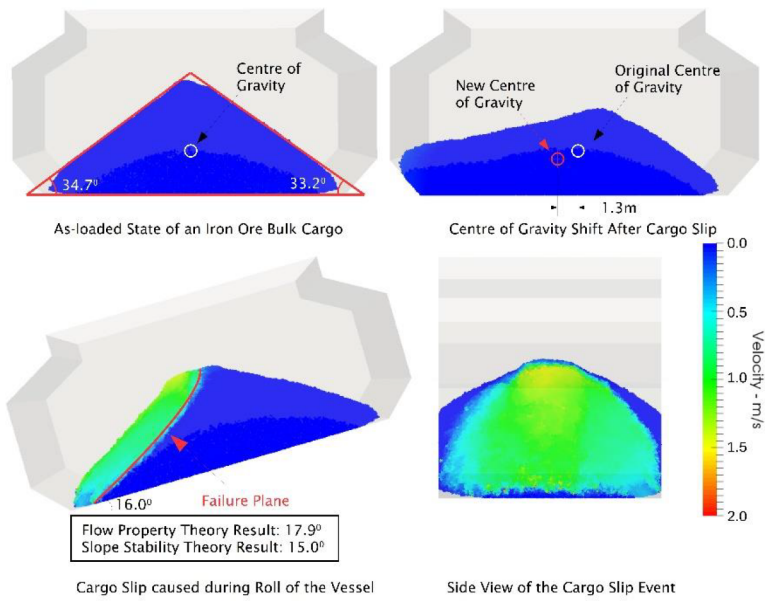
Table 2. Parameters used for all discrete element modelling calibration simulation.

Coefficient of Restitution - e	0.3
Poisson's Ratio - ν	0.3
Wall Friction - μ_w	0.3
Young's Modulus - Y	1e7 Pa
Time Step - Δt	1e-5 s

Table 3. Static roll angles modelling results using the flow property theory, the slope stability theory and DEM.

Modelling Method	Flow Property Theory	Slope Stability Theory	DEM
Static roll angle - Degrees	17.9	15	16

Graphical abstract



Highlights

- Bulk solids flow property theory can model iron ore cargo slip in maritime transport
- Cargo slip prediction with flow properties theory is close to soil mechanics theory
- Cargo slip model results from DEM is close to theoretical results.
- Precaution measures are required to prevent instabilities from cargo slip